



Hierarchical BiOCl microflowers with improved visible-light-driven photocatalytic activity by Fe(III) modification



Caijin Huang^{a,1}, Jinli Hu^{a,1}, Shan Cong^b, Zhigang Zhao^{b,*}, Xiaoqing Qiu^{a,*}

^a Research Institute of Photocatalysis, State Key Laboratory of Photocatalysis on Energy and Environment, College of Chemistry, Fuzhou University, Fuzhou 350002, China

^b Key Laboratory of Nanodevices and Applications, Suzhou Institute of Nanotech and Nanobionics, Chinese Academy of Science, 398 Ruoshui Road, Suzhou Industry Park, Suzhou 215123, China

ARTICLE INFO

Article history:

Received 12 January 2015

Received in revised form 27 February 2015

Accepted 1 March 2015

Available online 3 March 2015

Keywords:

BiOCl

Visible light

Surface modification

Multi-electron redox

Photocatalysis

ABSTRACT

Hierarchical BiOCl microflowers have been synthesized by one-step solvothermal method, which are constructed from many thin nanosheets by exposing the highly active highly active {001} facets. Considering the wide band gap of BiOCl microflowers (3.4 eV), the amorphous Fe(III) clusters were grafted on the surfaces through a simple impregnation method to extend the photocatalytic activity to the visible light region. The obtained products were characterized by X-ray diffraction, scanning electron and transmission microscopy, X-ray photoelectron spectroscopy, UV–vis diffuse reflectance spectroscopy, nitrogen adsorption–desorption, and electrochemical measurements. It is found that the Fe(III) clusters are just deposited on the surfaces rather than doped in the lattices of BiOCl. The morphologies and crystal structures of BiOCl microflowers thus remain unchanged after modification of Fe(III) clusters. The photocatalytic activity for the decomposition gaseous acetaldehyde can be significantly improved by the modification of Fe(III) clusters under visible light irradiation. The surface Fe(III) clusters play an important role in the interfacial charge transfer for the visible light absorption. Furthermore, together with the strong oxidative holes in the valence band of BiOCl, the Fe(III) clusters can serve as the redox reaction centers for the multi-electron reduction of oxygen molecules, resulting in the full decomposition of acetaldehyde into CO₂.

© 2015 Elsevier B.V. All rights reserved.

1. Introduction

The growing demand for the environmental remediation by photocatalysis needs to develop stable and effective photocatalytic materials, especially with high visible light activity, since the contaminated water and polluted air has become a widespread threat to public health [1,2]. Bismuth oxychloride (BiOCl) is one of the promising photocatalysts, featured with the tetragonal layered structures of [Bi₂O₂] slabs interleaved with double Cl slabs, endowed with an efficient separation of photoinduced charges [3,4]. Thus, considerable efforts have been devoted to prepare BiOCl nanostructures with a diversity of well-defined morphologies, such as nanosheets [4–6], nanoplates [7–9], and nanodisks [10], and nanoflakes [11]. Moreover, these nanostructures can act as the building blocks to self-assemble into three dimensional (3D)

hierarchical structures with superior photocatalytic performance. For instance, Zhang's group concluded that the degradation of Rhodamine B under ultraviolet light irradiation was much accelerated over the 3D hierarchical BiOCl compared to their common counterparts [12]. Song et al. found that the hierarchical BiOCl flowers assembled from thin nanoplates exhibited the enhanced photocatalytic activity for the decomposition of methyl orange under modeling sunlight [13]. Wang et al. further reported that the porous BiOCl microflowers composed of ultrathin nanosheets possessed higher photocatalytic performance via a photosensitization pathway under visible light illumination [14]. However, it should be noted that BiOCl belongs to the wide-band-gap semiconductor and can only be activated under ultraviolet light irradiation [3]. Therefore, it is imperative to develop efficient strategies to modify the BiOCl photocatalysts sensitive to visible light, considering about the potential applications in indoor or other surrounding without UV emission.

In fact, over the past decades, several strategies have been developed to extend the photocatalytic activity of wide-band-gap photocatalysts in the visible region, including the band-gap energy

* Corresponding authors. Tel.: +86 591 83969021; fax: +86 591 83969021.

E-mail addresses: zhao2011@sinano.ac.cn (Z. Zhao), qiuxq@fzu.edu.cn (X. Qiu).

¹ These authors contributed equally to this work.

tailoring by doping the exotic ions [15–20], coupling with a narrow band-gap semiconductor or colored dye [21,22], and surface deposition of noble metal nanoparticles with plasmon absorption [23–26]. However, the photocatalytic performances are still far from satisfactory, since the quantum efficiencies of these developed photocatalysts under visible light irradiation are much lower than those of their corresponding host wide band gap photocatalysts under UV light irradiation [27]. Recently, Irie et al. reported a new photocatalyst with visible light activity, the Cu(II) ion modified titanium oxide (TiO₂, rutile) [28]. Marakami et al. also prepared the similar photocatalysts by stirring TiO₂ in a metal chloride solution [29]. Such surface modification with transition metal ions, particularly Cu(II) or Fe(III) clusters, has been demonstrated as an efficient way to realize the visible photocatalytic capability of the wide gap band photocatalysts, mainly focusing on TiO₂-based materials [28,30–38]. The metal ions clusters are just fixed on the surfaces rather than doped in the lattices of the host semiconductor, thus not inducing the impurity levels in the band gap. The electron in the valence band of the host semiconductor can be promoted upon visible light excitation into these grafted surface clusters, that is, the interfacial charge transfer (IFCT) [39,40]. Consequently, the holes with strong oxidizing power generated in the valence band of the host semiconductor can decompose the organic pollutants, together with the surface grafted clusters involving the oxygen reduction [41,42], resulting in the high quantum efficiencies under visible light irradiation [36,43]. In our previous work, we extended this methodology to photocatalytically inactive α -Bi₂O₃ by surface constructing the amorphous Cu(II) clusters, and found that the obtained Cu(II)-Bi₂O₃ showed the significantly enhanced photocatalytic activity for the gaseous 2-propanol decomposition under visible light irradiation [44]. Therefore, it is reasonable to expect that the wide-band-gap BiOCl should become a visible light sensitive photocatalyst by surface modification with suitable metal ions. Herein, we prepared the 3D hierarchical BiOCl microflowers via a facile solvothermal method, and selected the Fe(III) ions as the modifier. It is found that the as-obtained Fe(III)-BiOCl exhibits the improved photocatalytic activity for decomposition of gaseous acetaldehyde to CO₂ under the visible light irradiation.

2. Experimental

2.1. Synthesis of BiOCl samples

The 3D hierarchical BiOCl microflowers were prepared by a solvothermal method using glycerol as the solvent. Typically, 0.4 mmol of Bi(NO₃)₃·5H₂O was dissolved in 76 mL of glycerol, and 0.4 mmol NaCl was dissolved into 4 mL of distilled water, respectively. Then the clear NaCl solution was added slowly into the Bi(NO₃)₃·5H₂O solution. After 30 min stirring, the resulting solution was transferred into a 100 mL Teflon-lined stainless steel autoclave, and solvothermally treated at 140 °C for 2–24 h when the reactions were complete, the autoclave was naturally cooled down to room temperature. The samples were collected by centrifugation, washed with distilled water and ethanol several times, and dried at 70 °C.

2.2. Modification of BiOCl sample with Fe(III) clusters

The grafting of Fe(III) cluster onto the surfaces of BiOCl was prepared by impregnation using FeCl₃·6H₂O as the source of Fe(III), similar to our previous reports about Cu(II) clusters modifications [43,44]. Briefly, 1 g of BiOCl sample was dispersed into 10 mL of FeCl₃ solution in a vial reactor, followed by adding a certain amount of HCl to adjust the pH to 2. The concentration of FeCl₃·6H₂O was set to be 0.484 g/L. The suspension was heated at 90 °C, stirred for

1 h in the vial reactor, and then filtered and washed with a sufficient amount of distilled water. The resulting residue was dried at 70 °C for 12 h, and subsequently grounded into fine powder using an agate mortar. The sample was denoted as Fe(III)-BiOCl.

2.3. Sample characterizations

The crystalline phases of the samples were identified by powder X-ray diffraction (XRD) on a Bruker D8 ADVANCE X-ray diffractometer in the diffraction angle (2θ) region of 10–70°, using Cu K α radiation as the source. The morphological and structural features of the samples were investigated on a Hitachi New Generation SU8010 field emission scanning electron microscope (FESEM), and transition electron microscopy (TEM) on a Hitachi HF-2000 instrument under an acceleration voltage of 200 KV. X-ray photoelectron spectroscopy (XPS) characterization was studied on a PerkinElmer model 5600 XPS system. The binding energy data are calibrated with the C 1s signal at 284.6 eV. The absorption spectra of the samples were obtained by the diffuse reflection method using a Lambda 950 UV/vis spectrophotometer. Nitrogen adsorption measurement was carried out at 77 K using a 3020 system utilizing Brunauer–Emmett–Teller (BET) calculation for surface areas.

2.4. Electrochemical measurements

The method for preparing the working electrode was described in detail in our previous works [9]. The electrolyte was 0.2 M Na₂SO₄ solution. A Xe-arc lamp with a 420 nm cutoff filter was employed as a visible light photosource, and the light intensity was set to be 100 mW/cm². The reactor was the three-electrode electrochemical cell including a working electrode, a platinum mesh counter electrode and a Ag/AgCl (3 M KCl) as reference electrode. The current-potential curves of the samples were conducted on an electrochemical workstation (CHI660E), and the electrolyte bubbled with oxygen gas for 1 h before the experiment. The flat-band potentials of the semiconductors were determined from the Mott–Schottky plots under three different frequencies on a BIOLOGIC VSP300 electrochemical workstation. Electrochemical impedance spectroscopy (EIS) experiments were carried out on a Zennium electrochemical workstation (Zahner, Germany). EIS observation was determined under AC polarization with the frequency range from 4 to 100 MHz at 0.4 V potential. The electrolyte bubbled with high purity argon for 1 h before the EIS experiments.

2.5. Evaluation of photocatalytic properties

The photocatalytic activities of photocatalysts were measured by the decomposition of gaseous acetaldehyde under visible light illumination using a sealed Pyrex glass photocatalytic reaction vessel (500 mL). In a typical steady-state experiment, thin film prepared by loading 50 mg of catalyst powder on a quartz disk with a diameter of ca. 2.5 cm were placed at the bottom of the reaction vessel. Fixed amount (0.1 mL) of an appropriate concentration of gaseous acetaldehyde (withdrawn from the saturated vapor over liquid acetaldehyde in a sealed bottle at 18 °C) was injected into the vessel. After adsorption-equilibrium was attained (approximately 1 h), visible light from a Xe-lamp (CEL-HXF300) with a 420 nm band pass filter was irradiated vertically onto the whole area of the catalyst film through a quartz plate window. The photodecomposition processes were followed by taking 1 mL of gas from the vessel with a syringe every 30 min, and the concentration of acetaldehyde and CO₂ product were measured by a gas chromatograph using acetaldehyde and CO₂ calibrating gas as references.

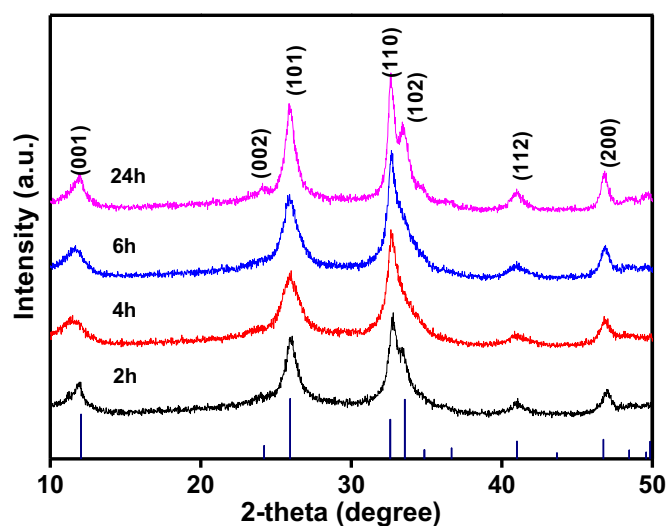


Fig. 1. XRD patterns of hierarchical BiOCl microflowers obtained at 140 °C for 2–24 h.

3. Results and discussion

Fig. 1 gives the XRD patterns of the samples obtained by the solvothermal treatment at 140 °C for given periods of time. For comparison, the standard diffraction data (JCPDS card No. 6-249) for bulk BiOCl as well as the corresponding Miller indices are also shown. As can be seen, all the diffraction peaks of the as-obtained samples can be assigned to the tetragonal matlockite BiOCl phase. No diffraction peaks corresponding to other impurities such as monoclinic Bi_2O_3 , orthorhombic $\text{Bi}_{12}\text{O}_{15}\text{Cl}_6$, or narrow band-gap Bi_2O_3 , are detected. Notably, the predominant peak at 32.6° corresponds to the (1 1 0) reflection, while the {001} facets exhibit rather weak diffraction intensity, suggesting the oriented growth of BiOCl along the [001] direction [45]. Furthermore, there is no obvious evolution of the intensity and width of the XRD peaks as prolonging the reaction time from 2 to 24 h, indicating the reaction time has negligible effect on the particle sizes and morphologies of the samples, which is confirmed by the SEM observations.

The representative SEM images of the samples after various solvothermal treatment times are shown in Fig. 2. It is clear that the BiOCl microflowers were produced on a large scale after the solvothermal reactions at 140 °C. The hierarchical BiOCl microflowers are very uniform in morphology with about 1 μm diameter, and composed of many thin nanosheets. The dimensional sizes of our hierarchical structures are close to the magnitude of the visible light wavelength. Thus, the enhancement effect induced by light scattering over the hierarchical structures can be expected, which in turn causes the light to be multiply absorbed during the photocatalysis process under visible light irradiation. The BiOCl microflowers remain unchanged in shape and particle size despite the different reaction times, which is in good agreement with the XRD analysis. In generally, BiOCl tends to form 2D nanoplates, nanodisks, or nanosheets, due to its intrinsic tetragonal layered structures [4]. In our study, the BiOCl nanosheets were formed by the hydrolysis of $\text{Bi}(\text{NO}_3)_3$ and reaction with Cl^- ions. The solvent glycerol is believed to promote the self-assembly of the nanosheets to form the 3D hierarchical microflowers [14]. Additionally, as shown in Fig. 3a, the typical TEM image of an individual microflower further reveals the hierarchical flower-like structures constructed by nanosheets with an average thickness of 6 nm. Fig. 3b gives the high resolution TEM (HRTEM) image of the thin nanosheets. The clear lattice fringes demonstrate the good crystallinity and single-crystal nature of these sheet-like subunits. In particular, the interplanar

spacing of 0.279 nm belongs to the separation between (1 1 0) lattice planes along the [001] direction, while the interplanar spacing of nanosheet thin lateral facets is determined to be 0.653 nm, corresponding to that of the two adjacent (001) planes. Based on the above XRD analysis and the symmetries of BiOCl, the hierarchical microflowers are constructed from the thin nanosheets being exposed by top and bottom {001} facets and lateral sides of {110} facets. Therefore, our prepared BiOCl microflowers possess a high percentage of highly active (001) facets [4], which is expected to act as the ideal platform for grafting the Fe(III) clusters and enhancing the photocatalytic activities.

Consequently, the 3D hierarchical BiOCl microflowers were modified by Fe(III) clusters to achieve the visible-light active Fe(III)–BiOCl photocatalysts. Because of the small amount of Fe(III), the XRD patterns of the Fe(III)–BiOCl (Fig. S1) show no characteristic diffraction peaks related to Fe_2O_3 , FeOOH, or other iron based compounds. Compared with the bare BiOCl, the Fe(III) modification did not induce any apparent shifting of XRD peaks, preliminarily implying that the Fe(III) clusters are dispersed on the surfaces rather than doped into the lattices of BiOCl. Moreover, the morphology of Fe(III)–BiOCl was kept almost the same as that of bare BiOCl microstructure (Fig. S2). The Fe(III) clusters were hardly to be observed on the surfaces of BiOCl microflowers, probably because of its small amount and good dispersion, which is similar to the cases of Fe(III) modified TiO_2 [31], Fe(III)–AgBr [46] and Fe(III)– Ag_3PO_4 [47]. In order to certify the existence of Fe(III) clusters, the elemental mapping of Fe(III)–BiOCl was conducted using SEM with an energy dispersive X-ray (EDX). The SEM-EDX elemental mapping results are shown in Fig. 4. Fig. 4a is a regular SEM image of Fe(III)–BiOCl, which clearly demonstrates the 3D hierarchical structures. The other images in Fig. 4 represent EDX mapping of Bi, Cl, and Fe elements, respectively. As can be seen, the Fe element is homogeneously distributed, besides the Bi and Cl elements, which provide the direct evidence for the good dispersion and attachment of Fe(III) clusters on the surfaces of microflowers.

In order to analyze the chemical compositions and specify the chemical states of surface elements of the samples, XPS measurements were further carried out. The survey spectrum of Fe(III)–BiOCl resembles that of bare BiOCl, which shows the strong signals of Bi, O, and Cl at the sample surfaces (Fig. S3). Fig. 5a gives the Bi 4f core-level spectra of the samples. Two intensive peaks at 164.68 and 159.38 eV are observed, which can be assigned to the $\text{Bi } 4f_{5/2}$ and $\text{Bi } 4f_{7/2}$ spin-orbital components of Bi^{3+} in BiOCl [10]. No photoelectron signals associated with Bi^{2+} , Bi^{4+} or Bi^{5+} states in bismuth oxides appeared, suggesting the high purity of the samples. As illustrated in the O 1s core level spectra (Fig. 5b), sharp peaks at 529.9 eV can be seen, which come from the Bi–O bond in BiOCl. On the other hand, the Cl 2p XPS spectra consist of well-defined Cl 2p_{3/2} and Cl 2p_{1/2} photolines that are located at 198.1 and 199.6 eV, respectively, consistent with the values for Cl^- in BiOCl reported in the literature [10]. Particularly, after Fe(III) clusters modification, no critical shifts of the peak positions are observed, indicating that the Fe(III) clusters were just fixed on the surfaces instead of doped into the lattices of BiOCl. These are ascribed to the fact that low temperature (90 °C) deposition of Fe(III) clusters does not have enough energy to impact the BiOCl natural structure. Encouragingly, after Fe(III) clusters modification, as displayed in Fig. 5d, weak iron 2p signals are detected. $\text{Fe } 2p_{3/2}$ and $\text{Fe } 2p_{1/2}$ peaks are located at approximately 710.6 and 723.5 eV, respectively. The energy difference between the two levels is about 13 eV, a value for the characteristic of Fe^{3+} state [48]. Yu et al. explored the details of the Fe(III) state on rutile TiO_2 by employing the XPS and X-ray absorption fine structure (XAFS) measurements and concluded that Fe(III) was grafted as amorphous $\text{FeO}(\text{OH})$ -like clusters [31]. Because of the similar experimental results to the case of Fe(III)– TiO_2 , the chemical state and environment of Fe(III) on the

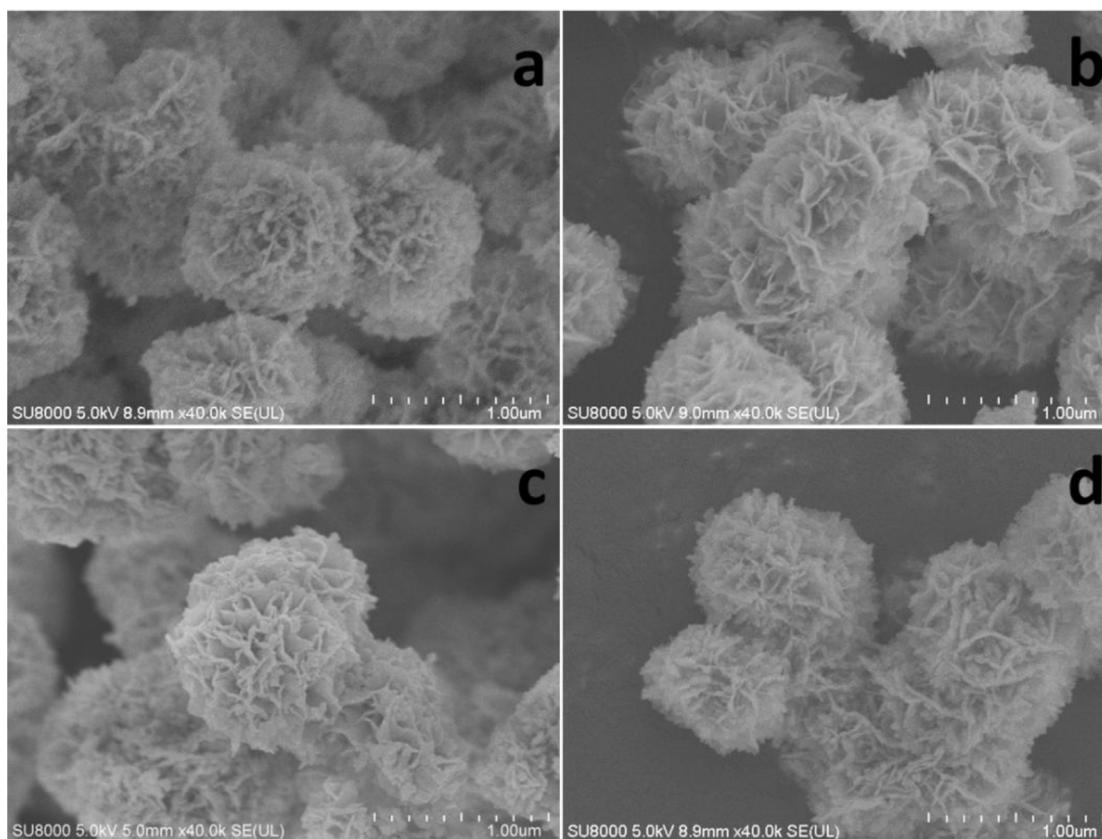


Fig. 2. Typical SEM images of hierarchical BiOCl microflowers obtained at 140 °C for 2–24 h, (a) 2 h, (b) 4 h, (c) 6 h, and (d) 24 h.

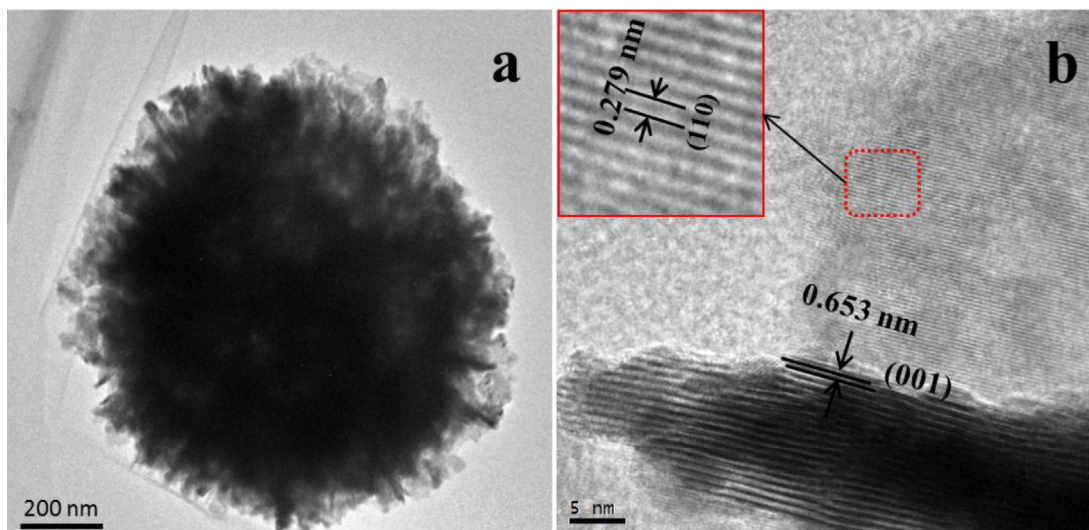


Fig. 3. (a) TEM image of single hierarchical BiOCl microflower, (b) HRTEM image of BiOCl.

3D hierarchical BiOCl microflowers can be described in the same way, amorphous iron oxyhydroxide clusters.

The optical properties of the samples were measured by the diffuse reflectance spectroscopy at room temperature. As depicted in Fig. 6, bare BiOCl microflowers show the characteristic absorption of wide-band gap semiconductor photocatalysts, an intense interband absorption at wavelength shorter than 370 nm. As BiOCl belongs to the indirect semiconductor, the bandgap energy was calculated to be 3.4 eV from the tangent lines in the plots of square root of the Kubelka–Munk function (Fig. S4). For the Fe(III)–BiOCl sample, it is clear that a new absorption appeared from 370 nm to

580 nm, besides the intrinsic band to band transition of BiOCl. The inset of Fig. 6 gives the differences of UV–vis spectra of bare BiOCl and Fe(III)–BiOCl. The additional absorption band in the visible light region could be ascribed to the interfacial charge transfer (IFCT) from the valence band of BiOCl to the surface grafted Fe(III) clusters [31,43]. The enhanced optical properties by IFCT are believed beneficial to photocatalytic activity under visible light irradiation.

In order to evaluate the photocatalytic activities of the obtained samples, the decomposition of gaseous acetaldehyde was next performed under visible light illumination, since acetaldehyde is generally used as the indicator of the volatile organic compounds

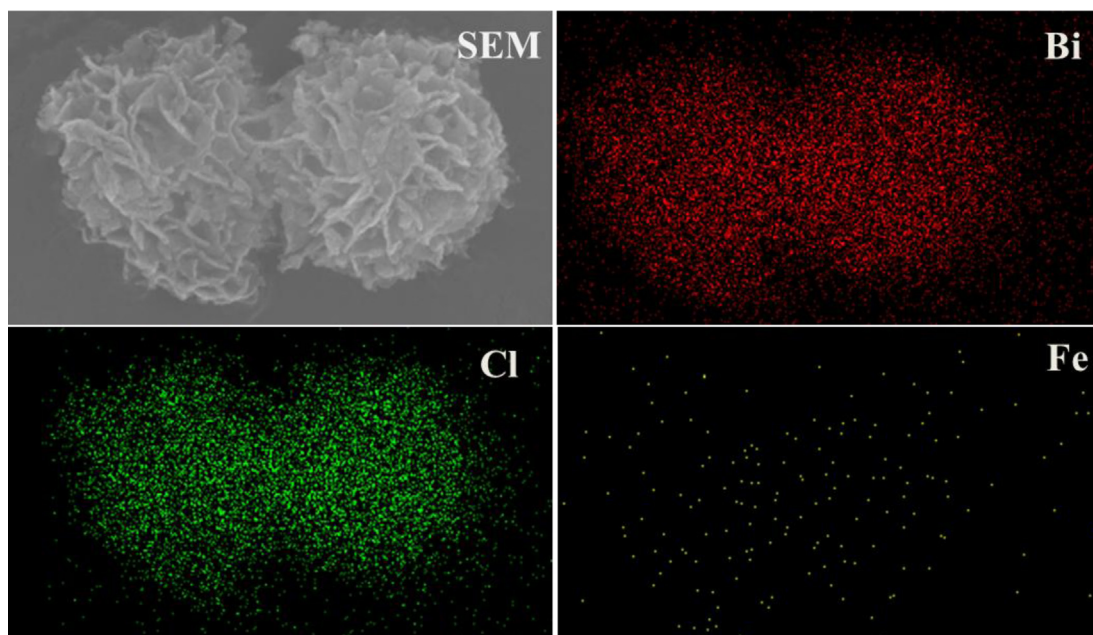


Fig. 4. Typical SEM images and the elemental mapping of Bi, Cl, Fe, of Fe(III)-BiOCl sample.

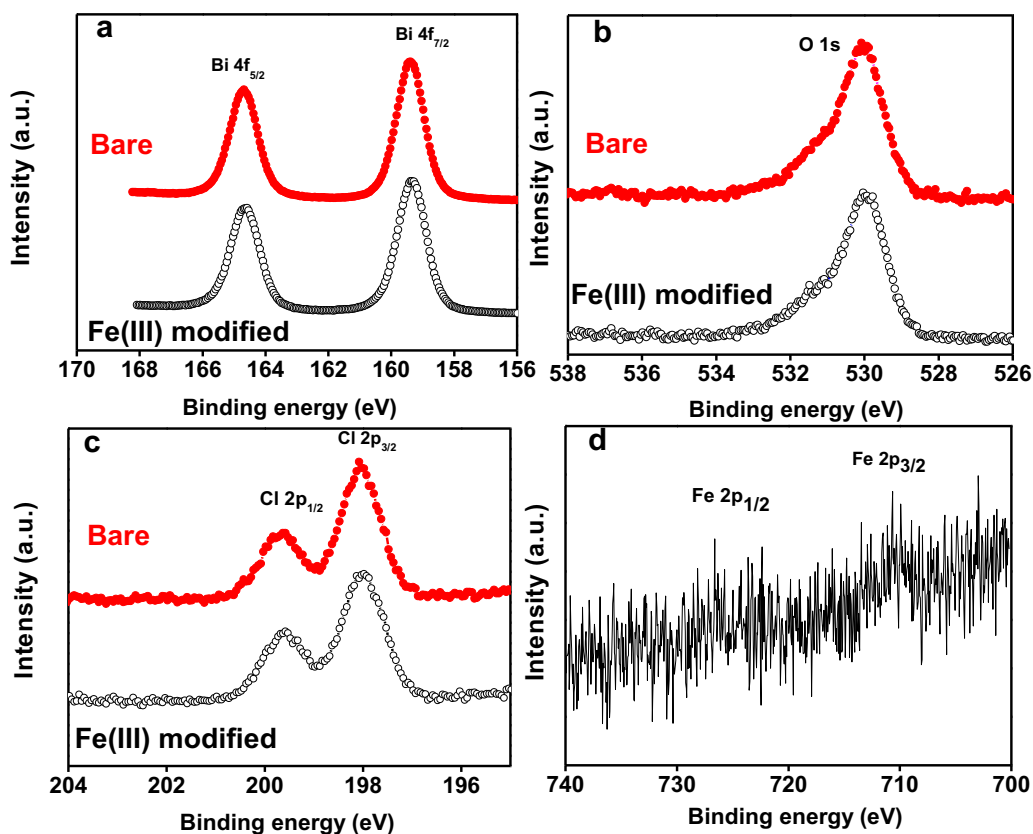


Fig. 5. XPS spectra for bare BiOCl and Fe(III)-BiOCl, (a) Bi 4f core-level spectra, (b) O 1s core-level spectra, (c) Cl 2p core-level spectra, and (d) Fe 2p core-level spectrum.

of indoor air [49]. Prior to the photocatalytic reaction, the photocatalysts were fully pre-illuminated with a Xe lamp to remove the surface absorbed organic contaminants. After the injection of gaseous acetaldehyde (about 100 ppm), the reaction vessel was kept in the dark for one hour to reach the adsorption/desorption equilibrium. The concentrations of acetaldehyde and CO_2 in the vessel were determined upon visible light irradiation for the

photocatalytic activity assessment. Fig. 7a shows the typical change in the concentrations of acetaldehyde and CO_2 over bare BiOCl microflowlers as a function of irradiation time. The concentration of acetaldehyde declines slowly, accompanying the production of small amount of CO_2 within 10 h irradiation. As discussed above, BiOCl microflowlers have large band gap energy of 3.4 eV. The limited photocatalytic activity of bare BiOCl may come from a

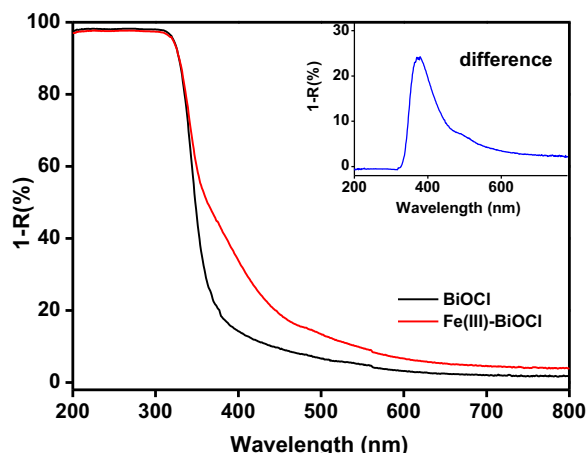


Fig. 6. UV-vis spectra of bare BiOCl and Fe(III)-BiOCl, inset: the difference UV-vis spectrum of bare BiOCl and Fe(III)-BiOCl.

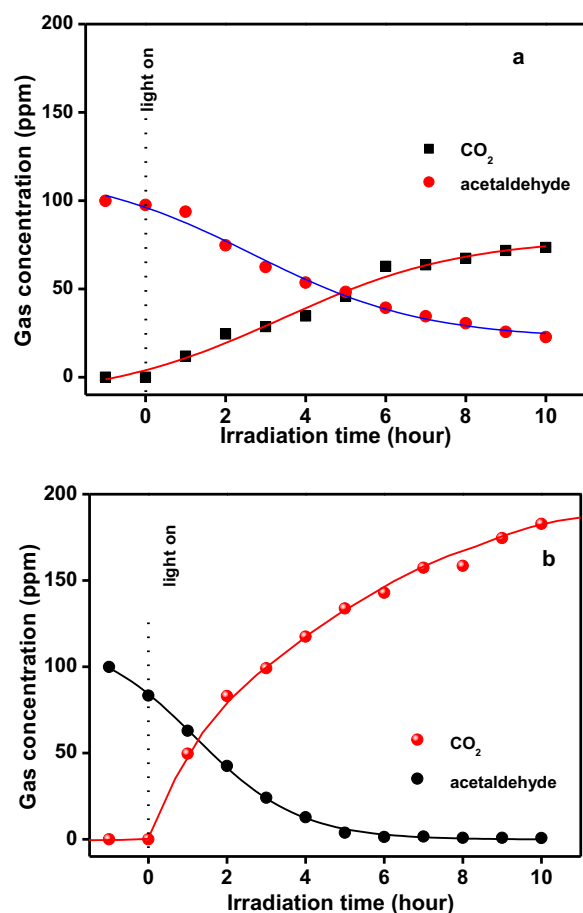


Fig. 7. Time-dependent gas concentration during gaseous acetaldehyde decomposition under visible light irradiation over various photocatalysts, (a) bare BiOCl and (b) Fe(III)-BiOCl.

small fraction of UV light leakage through the glass filter. In contrast, Fe(III)-BiOCl sample exhibits much improved photocatalytic activity compared with bare BiOCl under the identical irradiation condition. As shown in Fig. 7b, the acetaldehyde was almost removed completely after about 5 h irradiation. Meanwhile, the concentration of CO₂ increased sharply with the onset of visible light irradiation. After 10 h irradiation, the concentration of CO₂ in the vessel is closed to 200 ppm, double amount of the

initial acetaldehyde, indicating that the complete decomposition of acetaldehyde can be achieved over our Fe(III)-BiOCl sample ($\text{CH}_3\text{CHO} + 5/2\text{O}_2 \rightarrow 2\text{CO}_2 + 2\text{H}_2\text{O}$).

Generally speaking, the specific surface areas of photocatalysts play important roles in the promotion of photocatalytic activities. To understand the reasons behind the improved photocatalytic activity of Fe(III)-BiOCl, the effects of Fe(III) clusters modification on the surface areas and the pore structure of the samples are investigated by BET technique. Fig. 8 shows the N₂ adsorption-desorption isotherms for the bare BiOCl microflowers and Fe(III)-BiOCl. As can be seen, both bare BiOCl microflowers and Fe(III)-BiOCl exhibit type IV isotherms with a typical H₃ hysteresis loop characteristic of porous solids according to the IUPAC classification [50], implying the presence of the porous structures. The corresponding pore size distribution curve obtained by Barrett-Joyner-Halenda (BJH) method was shown in Fig. S5. The BET surface area and total pore volume of the bare BiOCl microflowers are determined to be 41.27 m²/g and 0.224 cm³/g, as well as 39.48 m²/g and 0.26 cm³/g for Fe(III)-BiOCl, respectively. The comparable values indicate that the specific surface areas and pore features cannot account for the enhancement of the photocatalytic activity by the Fe(III) clusters modification. In order to specify the role of Fe(III) clusters, we further performed the electrochemical measurements. Fig. 9a and b give the linear Mott-Schottky plots in the dark for bare BiOCl microflowers and Fe(III)-BiOCl. It is clear that the Fe(III) modification did not change the band edge potential of the BiOCl, because the Fe(III) clusters are just deposited on the surfaces, agreeable with the above SEM, TEM and XPS results. The flat band potential is about -1.3 V versus Ag/AgCl at pH 7, which is in good consistent with our previous report on BiOCl nanoplates [9]. According to the above UV-vis spectra analysis, we can calculate the valence band potentials of BiOCl is about 2.3 V, suggesting the sufficient oxidation ability of holes in the valence band to decompose the organic compounds. Fig. 9c depicts current-potential curves of the bare BiOCl and Fe(III)-BiOCl electrodes in the dark in the presence of oxygen. As for the bare BiOCl electrode in the presence of oxygen, the current was hardly observed in the potential range between 0 and 0.4 V. A small current was observed below 0 V, originating from the one-electron reduction of oxygen molecules ($\text{O}_2 + \text{H}^+ + \text{e}^- \rightarrow \text{HO}_2$, $E^0 = -0.046 \text{ V}$) [51]. The electron behavior in bare BiOCl electrode is very similar to that of bare TiO₂ reported by Kitano et al. [52]. Interestingly, the current is much enhanced for Fe(III)-BiOCl electrode compared with bare BiOCl electrode (Fig. 9c). Moreover, it can be clearly seen that the potential of the starting current shifted to the positive region (about 0.2 V) for Fe(III)-BiOCl electrode. It should be mentioned that this potential is not sufficient to initiate the one-electron reduction of oxygen molecules. Thus, the shifting of the starting potential and enhancement of the current should be related to the Fe(III) clusters on the BiOCl surfaces. It is reported that the redox potential for the Fe(III)/Fe(II) couple is strongly dependent upon the chemical state environment of iron ions [53]. The standard redox of Fe³⁺/Fe²⁺ under acidic condition (pH 0) is about 0.77 V [51]. At neutral condition, the iron ions generally exist as the insoluble compounds, such as iron hydroxides or hydroxide carbonates. The redox potential of Fe(OH)₃/Fe²⁺ is about -0.236 V, while that of Fe(OH)₃/FeCO₃ is about 0.2 V [53]. As the above discussion, the Fe(III) clusters can exist as the amorphous iron oxyhydroxide on the surfaces of BiOCl microflowers. In our study, the electrochemical measurements were conducted in a 0.2 M Na₂SO₄ electrolyte (pH 7). Therefore, the starting potential (0.2 V) should be related to the redox reaction of Fe(III) clusters, i.e., the electron transfer from the electrode to Fe(III) clusters and resulting in the formation of Fe(II) clusters. The resulting Fe(II) clusters have sufficient potential (0.2 V) to reduce oxygen molecules via a multi-electron reduction process (two electron reduction: $\text{O}_2 + 2\text{H}^+ + 2\text{e}^- \rightarrow \text{H}_2\text{O}_2$, $E^0 = 0.68 \text{ V}$, four-electron reduction: $\text{O}_2 + 4\text{H}^+ + 4\text{e}^- \rightarrow 2\text{H}_2\text{O}$, $E^0 = 1.23 \text{ V}$) [51],

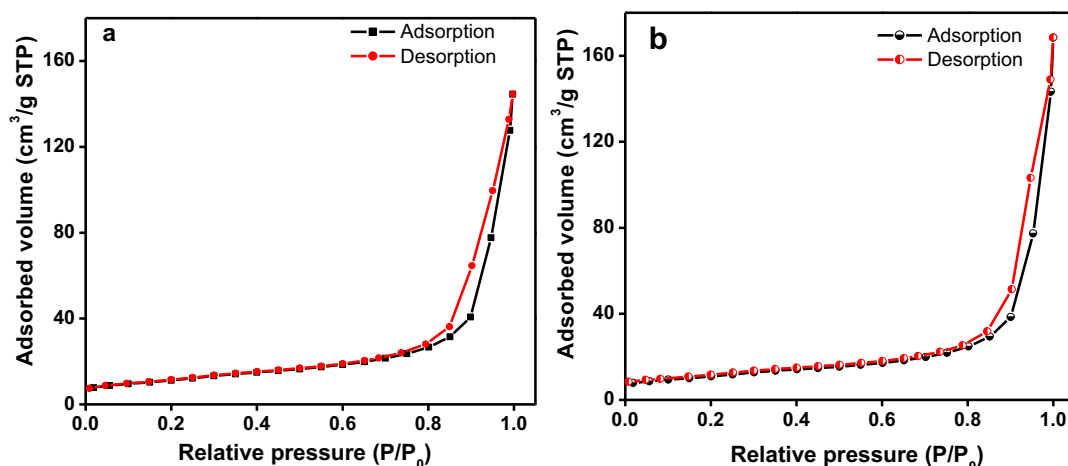


Fig. 8. Nitrogen adsorption-desorption isotherm of (a) the bare BiOCl and (b) the Fe(III)-BiOCl.

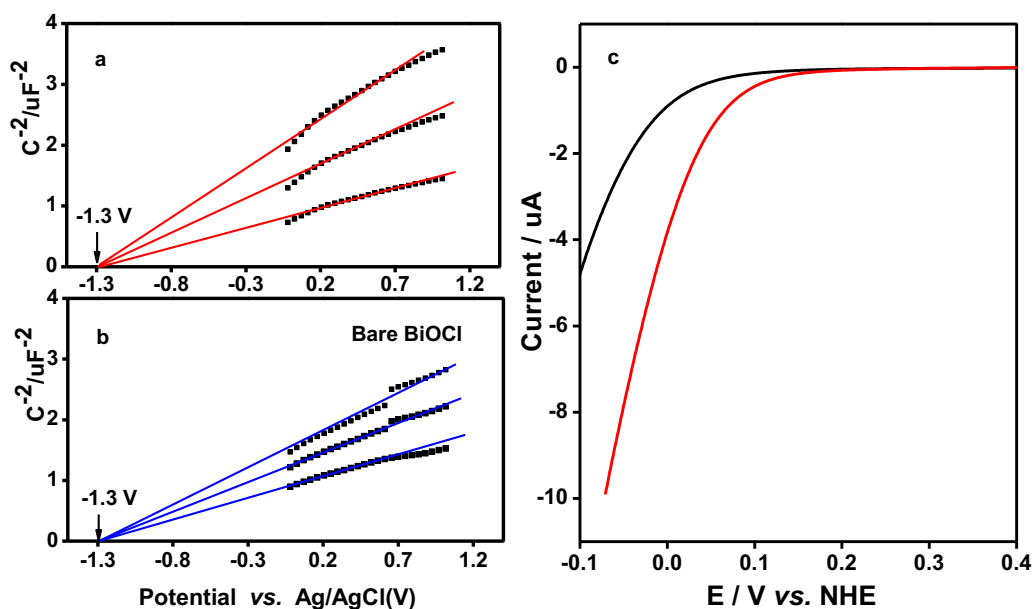


Fig. 9. Mott-Schottky plots for (a) Fe(III)-BiOCl and (b) bare BiOCl, (c) current-potential curves of bare BiOCl and Fe(III)-BiOCl electrodes under dark in the presence of O_2 .

and return to the Fe(III) clusters. In addition, the electrochemical impedance spectra (EIS) of the BiOCl and Fe(III)-BiOCl films were measured at 0.4 V in the dark and under visible light irradiation. As shown in Fig. S6, the Nyquist plot of bare BiOCl demonstrates its large charge transfer resistance. After Fe(III) modification, the property of the interfacial charge transfer is much improved, since the semicircle arc at high frequency region decreases evidently compared with bare BiOCl. Furthermore, the semicircle arc further reduces under visible light irradiation for Fe(III)-BiOCl electrode, suggesting that IFCT is beneficial for the electronic conductivity. Based on the above discussion, the photocatalytic mechanisms are proposed in Fig. 10. Namely, under visible light irradiation, the electrons in the valence band of BiOCl are excited and transferred to the surface grafted Fe(III) clusters through the IFCT process. The resulting Fe(II) clusters can serve as the multi-electron redox center for the oxygen reduction, and return to the initial states. Simultaneously, the holes in the valence band of BiOCl microflowers can decompose the acetaldehyde owing to their strong oxidation power. Therefore, the wide-band-gap BiOCl has been endowed with visible-light activity by surface modification of Fe(III) clusters.

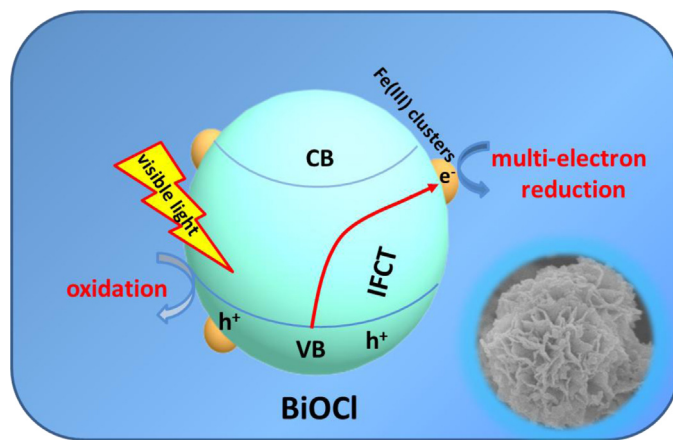


Fig. 10. Schematic illustration for the charge transfer and separation in the Fe(III)-BiOCl microflowers under visible light irradiation.

4. Conclusions

In summary, we have successfully fabricated hierarchical BiOCl microflowers via solvothermal method. The obtained samples possess large surface areas and big pore volumes, which are beneficial for the surface metal ions modifications. Through an impregnation method, amorphous Fe(III) clusters have been highly dispersed on the surfaces of the hierarchical BiOCl microflowers. The Fe(III) clusters induce negligible impact on the shapes and crystal structures of BiOCl microflowers. Encouragingly, the Fe(III)–BiOCl exhibits improved photocatalytic activity for decomposition of gaseous acetaldehyde under visible light irradiation. This can be ascribed to the fact that the Fe(III) clusters can facilitate the separation of photo-generated charge carriers through IFCT process under visible light irradiation, and act as the redox reaction centers for the multi-electron reduction of oxygen molecules. This work not only demonstrates the feasibility for the utilization of low-cost Fe(III) clusters to endow the wide-band-gap BiOCl with visible-light activity, but also paves a way for the rational design of visible light photocatalysts.

Acknowledgments

The Project Sponsored by the Scientific Research Foundation for the Returned Overseas Chinese Scholars, State Education Ministry. This work was also financially supported by the National Natural Science Foundation of China (NSFC, Grant Nos. 21273038, and 51372266), Natural Science Foundation of Jiangsu Province (BK20130348), and the Fund of Key Laboratory of Optoelectronic Materials Chemistry and Physics, Chinese Academy of Sciences (2008DP173016).

Appendix A. Supplementary data

Supplementary data associated with this article can be found, in the online version, at <http://dx.doi.org/10.1016/j.apcatb.2015.03.001>.

References

- [1] J. Zhang, D.L. Mauzerall, T. Zhu, S. Liang, M. Ezzati, J.V. Remais, *Lancet* 375 (2010) 1110–1119.
- [2] N. Bruce, R. Perez-Padilla, R. Albalak, *Bull. World Health Org.* 78 (2000) 1078–1092.
- [3] K.-L. Zhang, C.-M. Liu, F.-Q. Huang, C. Zheng, W.-D. Wang, *Appl. Catal. B: Environ.* 68 (2006) 125–129.
- [4] J. Jiang, K. Zhao, X. Xiao, L. Zhang, *J. Am. Chem. Soc.* 134 (2012) 4473–4476.
- [5] L. Ye, L. Zan, L. Tian, T. Peng, J. Zhang, *Chem. Commun.* 47 (2011) 6951–6953.
- [6] S. Weng, Z. Fang, Z. Wang, Z. Zheng, W. Feng, P. Liu, *ACS Appl. Mater. Interfaces* 6 (2014) 18423–18428.
- [7] J. Ma, X. Liu, J. Lian, X. Duan, W. Zheng, *Cryst. Growth Des.* 10 (2010) 2522–2527.
- [8] Y. Xie, F. Chang, C. Li, J. Chen, J. Luo, L. Li, X. Hu, *CLEAN – Soil, Air, Water* 42 (2014) 521–527.
- [9] J. Hu, W. Fan, W. Ye, C. Huang, X. Qiu, *Appl. Catal. B: Environ.* 158 (2014) 182–189.
- [10] X. Zhang, X.-B. Wang, L.-W. Wang, W.-K. Wang, L.L. Long, W.-W. Li, H.-Q. Yu, *ACS Appl. Mater. Interfaces* 6 (2014) 7766–7772.
- [11] Y. Li, J. Liu, J. Jiang, J. Yu, *Dalton Trans.* 40 (2011) 6632–6634.
- [12] K. Zhang, J. Liang, S. Wang, J. Liu, K. Ren, X. Zheng, H. Luo, Y. Peng, X. Zou, X. Bo, J. Li, X. Yu, *Cryst. Growth Des.* 12 (2011) 793–803.
- [13] J.-M. Song, C.-J. Mao, H.-L. Niu, Y.-H. Shen, S.-Y. Zhang, *CrystEngComm* 12 (2010) 3875–3881.
- [14] D.-H. Wang, G.-Q. Gao, Y.-W. Zhang, L.-S. Zhou, A.-W. Xu, W. Chen, *Nanoscale* 4 (2012) 7780–7785.
- [15] W. Choi, A. Termin, M.R. Hoffmann, *J. Phys. Chem.* 98 (1994) 13669–13679.
- [16] X. Qiu, L. Li, J. Zheng, J. Liu, X. Sun, G. Li, *J. Phys. Chem. C* 112 (2008) 12242–12248.
- [17] X. Qiu, G. Li, X. Sun, L. Li, X. Fu, *Nanotechnology* 19 (2008) 215703.
- [18] R. Asahi, T. Morikawa, T. Ohwaki, K. Aoki, Y. Taga, *Science* 293 (2001) 269–271.
- [19] H. Yamashita, M. Harada, J. Misaka, M. Takeuchi, K. Ikeue, M. Anpo, *J. Photochem. Photobiol. A: Chem.* 148 (2002) 257–261.
- [20] S. Anandan, N. Ohashi, M. Miyauchi, *Appl. Catal. B: Environ.* 100 (2010) 502–509.
- [21] C. Chen, W. Ma, J. Zhao, *Chem. Soc. Rev.* 39 (2010) 4206–4219.
- [22] Y. Bessekhoud, D. Robert, J.V. Weber, *Catal. Today* 101 (2005) 315–321.
- [23] V. Subramanian, E.E. Wolf, P.V. Kamat, *J. Am. Chem. Soc.* 126 (2004) 4943–4950.
- [24] Z. Zheng, B. Huang, X. Qin, X. Zhang, Y. Dai, M.-H. Whangbo, *J. Mater. Chem.* 21 (2011) 9079–9087.
- [25] X. Zhou, G. Liu, J. Yu, W. Fan, *J. Mater. Chem.* 22 (2012) 21337–21354.
- [26] A. Bumajdad, M. Madkour, *Phys. Chem. Chem. Phys.* 16 (2014) 7146–7158.
- [27] H. Irie, Y. Watanabe, K. Hashimoto, *J. Phys. Chem. B* 107 (2003) 5483–5486.
- [28] H. Irie, S. Miura, K. Kamiya, K. Hashimoto, *Chem. Phys. Lett.* 457 (2008) 202–205.
- [29] N. Murakami, T. Chiyoya, T. Tsubota, T. Ohno, *Appl. Catal. A: Gen.* 348 (2008) 148–152.
- [30] H. Yu, H. Irie, K. Hashimoto, *J. Am. Chem. Soc.* 132 (2010) 6898–6899.
- [31] H. Yu, H. Irie, Y. Shimodaira, Y. Hosogi, Y. Kuroda, M. Miyauchi, K. Hashimoto, *J. Phys. Chem. C* 114 (2010) 16481–16487.
- [32] X. Qiu, M. Miyauchi, K. Sunada, M. Minoshima, M. Liu, Y. Lu, D. Li, Y. Shimodaira, Y. Hosogi, Y. Kuroda, K. Hashimoto, *ACS Nano* 6 (2011) 1609–1618.
- [33] M. Liu, X. Qiu, M. Miyauchi, K. Hashimoto, *Chem. Mater.* 23 (2011) 5282–5286.
- [34] M. Liu, X. Qiu, M. Miyauchi, K. Hashimoto, *J. Am. Chem. Soc.* 135 (2013) 10064–10072.
- [35] M. Liu, X. Qiu, K. Hashimoto, M. Miyauchi, *J. Mater. Chem. A* 2 (2014) 13571–13579.
- [36] M. Liu, R. Inde, M. Nishikawa, X. Qiu, D. Atarashi, E. Sakai, Y. Nosaka, K. Hashimoto, M. Miyauchi, *ACS Nano* 8 (2014) 7229–7238.
- [37] H. Irie, K. Kamiya, T. Shibanuma, S. Miura, D.A. Tryk, T. Yokoyama, K. Hashimoto, *J. Phys. Chem. C* 113 (2009) 10761–10766.
- [38] P. Wang, Y. Xia, P. Wu, X. Wang, H. Yu, J. Yu, *J. Phys. Chem. C* 118 (2014) 8891–8898.
- [39] C. Creutz, B.S. Brunshwig, N. Sutin, *J. Phys. Chem. B* 110 (2006) 25181–25190.
- [40] C. Creutz, B.S. Brunshwig, N. Sutin, *J. Phys. Chem. B* 109 (2005) 10251–10260.
- [41] Y. Nosaka, S. Takahashi, Y. Mitani, X. Qiu, M. Miyauchi, *Appl. Catal. B: Environ.* 111–112 (2012) 636–640.
- [42] M. Nishikawa, R. Takanami, F. Nakagoshi, H. Suizu, H. Nagai, Y. Nosaka, *Appl. Catal. B: Environ.* 160–161 (2014) 722–729.
- [43] X. Qiu, M. Miyauchi, H. Yu, H. Irie, K. Hashimoto, *J. Am. Chem. Soc.* 132 (2010) 15259–15267.
- [44] J. Hu, H. Li, C. Huang, M. Liu, X. Qiu, *Appl. Catal. B: Environ.* 142 (2013) 598–603.
- [45] W.Q. Fang, J.Z. Zhou, J. Liu, Z.G. Chen, C. Yang, C.H. Sun, G.R. Qian, J. Zou, S.Z. Qiao, H.G. Yang, *Chem. – Eur. J.* 17 (2011) 1423–1427.
- [46] H. Yu, L. Xu, P. Wang, X. Wang, J. Yu, *Appl. Catal. B: Environ.* 144 (2014) 75–82.
- [47] H. Yu, G. Cao, F. Chen, X. Wang, J. Yu, M. Lei, *Appl. Catal. B: Environ.* 160–161 (2014) 658–665.
- [48] L. Dghoughi, B. Elidrissi, C. Bernede, M. Addou, M.A. Lamrani, M. Regragui, H. Erguig, *Appl. Surf. Sci.* 253 (2006) 1823–1829.
- [49] Z.G. Zhao, M. Miyauchi, *Angew. Chem.* 120 (2008) 7159–7163.
- [50] K.S. Sing, *Pure Appl. Chem.* 57 (1985) 603–619.
- [51] A.J. Bard, R. Parsons, J. Jordan, *Standard Potentials in Aqueous Solution*, CRC press, 1985.
- [52] S. Kitano, N. Murakami, T. Ohno, Y. Mitani, Y. Nosaka, H. Asakura, K. Teramura, T. Tanaka, H. Tada, K. Hashimoto, *J. Phys. Chem. C* 117 (2013) 11008–11016.
- [53] F. Widdel, S. Schnell, S. Heising, A. Ehrenreich, B. Assmus, B. Schink, *Nature* 362 (1993) 834–836.